Successive homoclinic tangencies to a limit cycle

P. Hirschberg [a], Carlo Laing [b,1]

[a] *Department of Physics, University of California at Berkeley, Berkeley, CA 94720, USA*
[b] *Department of Physics, University of Auckland, Private Bag 92019, Auckland, New Zealand*

Abstract

The dynamics near a perturbed degenerate homoclinic connection to a periodic orbit in three dimensions is modeled by a two-parameter map. One parameter controls the passage of the manifolds of the orbit through one another, and the other breaks the degeneracy and causes the manifolds to intersect transversely. An analysis of the map recovers the results of Gaspard and Wang (1987), relating to the accumulation of saddle-node bifurcations of periodic orbits on a single homoclinic tangency, and in addition shows that the local behavior of these orbits at the two tangencies can be linked together giving closed loops in period versus parameter plots. These analytic results are then compared with numerical results from a three-dimensional system of ordinary differential equations.

1. Introduction

A homoclinic tangency to a periodic orbit in three dimensions is responsible for complicated recurrent dynamics. Specifically, a countable infinity of periodic orbits appear in a cascade of saddle-node bifurcations as the stable and unstable manifolds of a limit cycle approach a quadratic tangency in a one-parameter system. For details see the work by Gaspard and Wang [4], Gavrilov and Šil'nikov [5,6], Newhouse [13], or the summaries by Guckenheimer and Holmes [9], and Wiggins [14].

Most of these investigations have concentrated on a *single* quadratic tangency between the unstable and stable manifolds of the periodic orbit, and have derived results that are local in both parameter and phase

space. However, in a one-parameter system, the complete passage of the stable and unstable manifolds through each other often yields *two* successive tangencies, the 'leading' and 'trailing' tangencies, at two different values of the parameter. The local results referred to above can be applied to each tangency separately, but in general the manner in which the orbits created at one tangency connect with those associated with the other is problem specific and must be addressed numerically.

However, in some limited instances by varying a second parameter one can bring the two tangencies together and link up the local results about each tangency. We address one such situation. We consider perturbations of a degenerate homoclinic tangency to a saddle limit cycle with positive multipliers. The unperturbed system has a cycle with unstable and stable manifolds which coincide without intersecting transversely. The perturbations we consider cause the man-
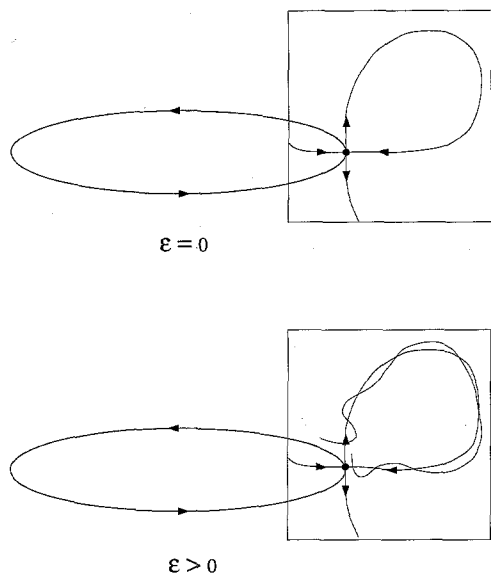
$\varepsilon = 0$

$\varepsilon > 0$

Fig. 1. A sketch of the arrangement of the manifolds of the periodic orbit on a surface of section for $\epsilon = 0$ (above), and ϵ non-zero (below).

ifolds to buckle (intersecting transversely) and hence split the single degenerate tangency into two (see Fig. 1). We construct a two-parameter return map modeling this situation. One parameter, μ, is used to control the passage of the manifolds through one another, while the other, ϵ, is used to break the degeneracy and cause the manifolds to intersect transversely. We analyze the fixed points of the resulting map and find that in the plot of cycle period versus μ a countable number of saddle-node bifurcations converge on each tangency, as in Gaspard and Wang [4]. In addition, because ϵ is small the map predicts how the cycles born near one tangency connect to those at the other. We find in the period versus μ plot that the periodic orbits created in saddle-node bifurcations at the separate tangencies link together to form closed bubbles.

An example of the degenerate cycle arises in the flow studied by Laing [12]. The author studies the effects of perturbations that break the axisymmetry of the normal form of the saddle-node/Hopf bifurcation [9]. In the symmetric flow a two-torus collides in a global bifurcation with a single large amplitude limit cycle. At the collision the unstable and stable manifolds of the cycle coincide without transverse intersec-

tions. Perturbations which break the axisymmetry of the flow cause the manifolds to intersect transversely. Two successive tangencies now occur and mode locking on the torus is observed. Numerical investigations by Laing [12] indicate that the boundaries of the resonance tongues (curves of saddle-node bifurcations) associated with the torus accumulate upon the two homoclinic tangencies to the cycle. We present additional numerics on this flow which further support the conclusions derived from our model map. We anticipate that cycles with this weakly broken degeneracy (and similar situations such as in Kirk [11]) will arise commonly near saddle-node/Hopf bifurcations and other related codimension-two points, and that the approach we follow here will be useful in understanding their respective dynamics.

2. Map construction

We consider a two-parameter family of vector fields in $\mathbb{R}^3$. When parameters $(\mu, \epsilon) = (0,0)$ the phase space flow possesses a limit cycle in which one branch of the stable manifold coincides with one branch of the unstable manifold. The cycle is unstable with multipliers $\lambda_u > 1$ and $0 < \lambda_s < 1$. We consider a small return plane Σ which is pierced transversely by the cycle at a single point. We take this point as the origin of a coordinate system (x, y) on the return plane with x measured along the local stable manifold and y along the unstable one as depicted in Fig. 2. Near the origin $(x, y) = (0, 0)$ the flow induces a return mapping that we approximate by the linear map $L : \Sigma \to \Sigma$

$$x \to \lambda_s x, \qquad y \to \lambda_u y. \tag{1}$$

We define two additional return sections Σ_a and Σ_b each lying in Σ:

$$\Sigma_a = \{ (x,y) \mid -\delta < x < \delta, \; y_0 \leq y \leq \lambda_u y_0 \},$$
$$\Sigma_b = \{ (x,y) \mid \lambda_s x_0 \leq x \leq x_0, \; -\delta < y < \delta \}, \tag{2}$$

where x_0, y_0, and δ are small constants greater than zero (see Fig. 2).

Our goal is to construct an approximate return map on Σ_a that models the dynamics of the flow. The return
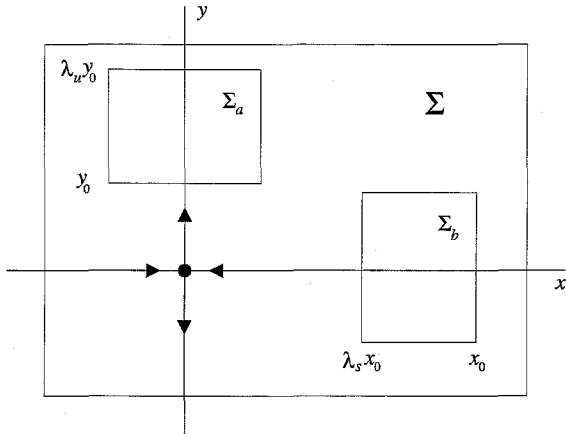
Fig. 2. The limit cycle pierces the section Σ at $(x, y) = (0, 0)$. The unstable manifold lies along $x = 0$, while the stable manifold lies along $y = 0$. The linear flow takes points on Σ_b to Σ_a; the global flow takes points from Σ_a to Σ_b.

map is constructed by composing two maps, a global map and a local map. The global map, G, takes points on Σ_a to Σ_b while the local map L takes points on Σ_b back to Σ_a. This is a common approach used widely throughout the literature (see [14]). Often the local map is taken to be the linear approximation to the map induced by the flow near the limit cycle (as done in [4] and as we have done in Eq. (1)). The global map typically is approximated by a Taylor expansion about the unstable manifold (points on Σ_a near the intersection of the unstable manifold with Σ_a (the y-axis) follow the manifold to Σ_b).

Although our local map is the usual linear approximation, the construction of our global map differs considerably from the usual approach. Because we are interested in relating orbits associated with two tangencies, it will be necessary to consider behavior of our maps on the boundaries of the return sections. In previous works the dynamics of the return maps studied do not encounter the section boundaries and the complications that result do not arise. These additional complications limit our ability to construct an explicit map G of the most general nature; however we do construct one example map G that exhibits the essential geometric features one would expect for the situation we consider. Before constructing our global map, we discuss these boundary conditions.

2.1. Boundary conditions

An important feature of the definition of the return sections Σ_a and Σ_b is that the linear map L takes the lower boundary $y = y_0$ of Σ_a to its upper boundary $y = \lambda_u y_0$, while L takes the right boundary $x = x_0$ of Σ_b onto its left boundary $x = \lambda_s x_0$. Thus a point $A = (x, y_0) \in \Sigma_a$ belongs to the same orbit as the point $B = (\lambda_s x, \lambda_u y_0)$ on the upper boundary, i.e. $L(A) = B$, and a similar correspondence occurs on Σ_b.

We wish to ensure that the related boundary points A and B remain on the same orbit under the global map G. In general the entire lower boundary curve $y = y_0$ of Σ_a under G will form a curve on Σ intersecting the x-axis at the point we have labeled $(x_0, 0)$. For the construction of our model map we assume that for small enough δ this curve can be taken vertical to coincide with our definition of the right boundary $x = x_0$ of Σ_b. Thus $G(A)$ lies on the $x = x_0$ boundary and its iterate $LG(A)$ under the local map lies on the left boundary $x = \lambda_s x_0$. The point $B = L(A)$ on Σ_a must get mapped under G to the left boundary point $LG(A) \in \Sigma_b$, or

$$LG(A) = GL(A),\tag{3}$$

for all boundary points $A = (x, y_0) \in \Sigma_a$. This is our first boundary condition.

The map G also must satisfy a boundary condition on its first derivative. Consider a tangent vector $v(A)$ in the tangent space ($\mathbb{R}^2$) of the point A. Under the local map the vector is mapped to $v(B) = D_X L \cdot v(A) = L \cdot v(A)$ at the point B, where $D_X L$ ($= L$) is the linear part of L. Under the global map G, vectors $v(A)$ and $v(B)$ become respectively vectors $D_X G|_A \cdot v(A)$ and $D_X G|_B \cdot v(B)$ in the respective tangent spaces of the points $G(A)$, $G(B) \in \Sigma_b$. (Here $D_X G|_A$ and $D_X G|_B$ are the linear part of G, evaluated at A and B, respectively.) We would like the vector $D_X G|_A \cdot v(A)$ at the right boundary point $G(A)$ of Σ_b to be mapped under L to $D_X G|_B \cdot v(B)$ at the left boundary point $G(B)$, or

$$D_X G|_B \cdot v(B) = L D_X G|_A \cdot v(A).\tag{4}$$

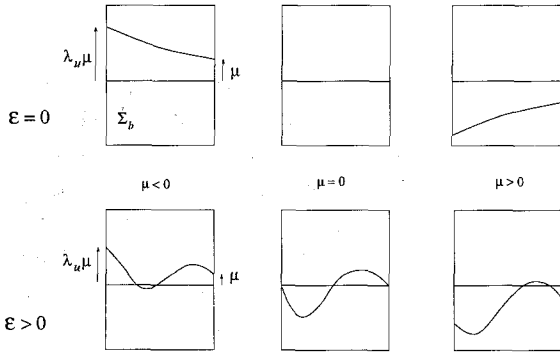Since $v(B) = L \cdot v(A)$ and $B = L(A)$ this requirement becomes our second boundary condition

Fig. 3. The behavior of the intersection of the unstable manifold with Σ_b. The parameter $\epsilon = 0$ for the upper three sections, while $\epsilon > 0$ below. The parameter μ is positive for sections on the left while negative on the right.

$$D_X G|_{L(A)} L = L D_X G|_A \,, \tag{5}$$

for all boundary points $A = (x, y_0) \in \Sigma_a$.

2.2. The global map

We now construct an example global mapping $G : \Sigma_a \rightarrow \Sigma_b$ in two steps. We first consider how the intersection of the unstable manifold with Σ_a (i.e. the curve $x = 0$) is mapped to the section Σ_b and how this mapping depends on the parameters μ and ϵ. We then consider how points on Σ_a near the unstable manifold are mapped to Σ_b.

2.3. Mapping the unstable manifold

The manner in which the unstable manifold is mapped from Σ_a to Σ_b under G depends upon the parameters (μ, ϵ) as illustrated in Fig. 3. The parameter μ provides a measure of the separation or splitting between the stable and unstable manifolds on the section Σ_b. The unstable manifold intersects Σ_a along the y-axis between y_0 and $\lambda_u y_0$ and we require G to take the lower end point $(0, y_0)$ in Σ_a to the right boundary point (x_0, μ) of Σ_b. Thus μ behaves as a splitting parameter. The map G should also maintain the identification of the end points $(0, y_0)$ and $(0, \lambda_u y_0)$ as points of the same trajectory. Since L takes (x_0, μ) on Σ_b to $(\lambda_s x_0, \lambda_u \mu)$ also on Σ_b, the map G must take the upper end point $(0, \lambda_u y_0) \in \Sigma_a$

to the left boundary point $(\lambda_s x_0, \lambda_u \mu) \in \Sigma_b$. This is accomplished if G satisfies the boundary condition (4).

The mapping of the remaining points of the y-axis on Σ_a to Σ_b by G depends upon ϵ in the following manner. When $\epsilon = 0$ we assume that as μ approaches zero the unstable manifold approaches a "flat" tangency with the stable manifold, and at $\mu = 0$ the two manifolds coincide. When $\epsilon \neq 0$ we assume the unstable manifold buckles in a simple manner producing two successive tangencies with variable μ (one could imagine and consider more complicated deformations giving rise to additional tangencies). Fig. 3 depicts this behavior on Σ_b.

The construction of G begins by focusing on its mapping of the unstable manifold from Σ_a to the section Σ_b incorporating the desired (μ, ϵ) dependence. We parametrize the intersection of the unstable manifold with Σ_b as

$$\begin{aligned} x_b &= \phi(y_a) \,, \\ y_b &= \mu y_a / y_0 + \epsilon f(y_a) \,, \end{aligned} \tag{6}$$

where $(0, y_a) \in \Sigma_a$, $(x_b, y_b) \in \Sigma_b$, and $\phi(y)$ and $f(y)$ are non-linear functions. The function $\phi(y)$ should decrease monotonically from x_0 to $\lambda_s x_0$ as y varies from y_0 to $\lambda_u y_0$, and following the application of Eq. (4) to Eq. (7) at the boundary point $A = (0, y_0)$, we obtain the boundary conditions

$$\phi(y_0) = x_0 \,, \quad \phi(\lambda_u y_0) = \lambda_s x_0 \,,$$
$$f(\lambda_u y_0) = \lambda_u f(y_0) \,. \tag{7}$$

The remaining condition (6) provides further boundary constraints on $\phi(y)$ and $f(y)$,

$$\phi'(\lambda_u y_0) / \phi'(y_0) = \lambda_s / \lambda_u \,, \tag{8}$$

$$f'(\lambda_u y_0) = f'(y_0) \,. \tag{9}$$

In order to maintain μ as a splitting parameter when ϵ is non-zero in Eq. (7), we further restrict our attention to functions $f(y)$ which satisfy, in addition to Eqs. (8) and (10), the following:

$$f(y_0) = f(\lambda_u y_0) = 0 \,. \tag{10}$$

To ensure two successive tangencies we consider functions $f(y)$ which have a single quadratic maximum

and minimum on the interval $[y_0, \lambda_u y_0]$, as for example,

$$f(y) = \sin\{2\pi(y - y_0)/(y_0\lambda_u - y_0)\}, \qquad (11)$$

and assume the extrema are not on the boundaries so that $f'(y_0) \neq 0$ and $f'(\lambda_u y_0) \neq 0$.

To obtain an example function $\phi(y)$ satisfying the above boundary conditions we begin by looking for a function ϕ which takes all the points $\lambda_u^n y_0$ along the y-axis to the corresponding points $\lambda_s^n x_0$ along the x-axis, i.e. $\phi(\lambda_u^n y_0) = \lambda_s^n x_0$ for each integer n. A particularly simple function is $\phi(y) = \lambda_s^n x_0\, y/(\lambda_u^n y_0)$ where we think of n as a function of y such that $y = \lambda_u^{n(y)} y_0$. To get values for $\phi(y)$ between the boundary points we generalize n to take on continuum values,

$$\phi(y) = x_0 \left(\lambda_s/\lambda_u\right)^{n(y)} y/y_0,$$
$$n(y) \equiv \log(y/y_0)/\log\lambda_u. \qquad (12)$$

We emphasize that for our global map we are only concerned with values of n between 0 and 1. We merely hope that the function ϕ which takes all discrete points $\lambda_u^n y_0$ along the y-axis to corresponding points along the x-axis might provide the desired stretching behavior on the smaller continuous interval $(y_0, \lambda_u y_0)$. In fact the function so constructed satisfies relation (8) and upon calculating the derivative,

$$\phi'(y) = \frac{\phi(y)}{y} \frac{\log\lambda_s}{\log\lambda_u}, \qquad (13)$$

we see that relation (10) is also satisfied.

The mapping (7) of the unstable manifold to Σ_b has the desired geometric properties. For non-zero ϵ the variation of μ through zero gives rise to two successive tangencies, while for zero ϵ the system approaches the degenerate tangency where the two manifolds coincide. Further, behavior at the $x = x_0$ and $x = \lambda_s x_0$ boundaries of Σ_b is consistent with condition (4) in that the linear flow L maps the right boundary intersection point of the unstable manifold to the intersection on the left (satisfying a slope boundary condition given by Eq. (6)).
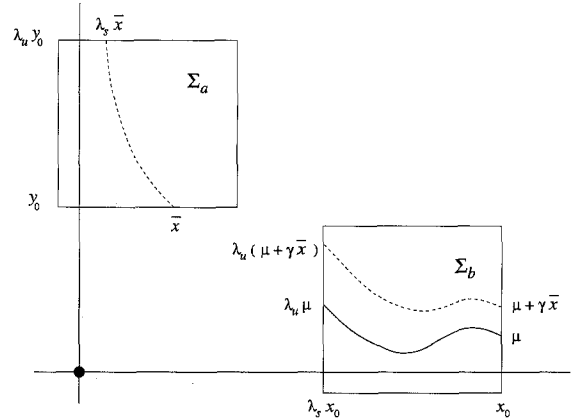

Fig. 4. One of a family of curves given by (15) parametrized by the intercept $\bar{x}$ is shown (dashed curve) on Σ_a. The curve under the global map (16) is mapped to a curve which lies above the unstable manifold (solid curve) on Σ_b.

2.4. Completing the global map

We now incorporate into G the ability to map points $(x_a, y_a) \in \Sigma_a$ near the unstable manifold to the section Σ_b. Rather than focusing on individual points (x_a, y_a), it is geometrically beneficial to consider curves in Σ_a. Consider the following decomposition of Σ_a into curves parametrized by their intersections with the boundary $y = y_0$ at the point $(\bar{x}, y_0)$. See Fig. 4. The curve with intercept $(\bar{x}, y_0)$ intersects the upper boundary $y = \lambda_u y_0$ at the point $(\lambda_s \bar{x}, \lambda_u y_0)$. An equation of the curve through these end points and others of the form $(\lambda_s^n \bar{x}, \lambda_u^n y_0)$ is

$$x = \bar{x} \left(\lambda_s/\lambda_u\right)^{n(y)} y/y_0, \qquad (14)$$

where $n(y)$ is defined in (13). For each value of $\bar{x}$, Eq. (15) produces a curve on Σ_a with end points $A(\bar{x}) = (\bar{x}, y_0)$ and $B(\bar{x}) = (\lambda_s \bar{x}, \lambda_u y_0)$ which lie on the same trajectory, i.e. $L(A) = B$. Further, for each (x_a, y_a) near the unstable manifold on Σ_a there is a unique curve passing though it possessing an intercept $\bar{x}$.

We now adjust the map for the unstable manifold (7) to map in addition the nearby curves (15) and hence nearby points. We need the resulting map G to behave properly at the boundaries. In particular $G(A)$ should be on the right ($x_b = x_0$) boundary of Σ_b while $G(B)$ should lie on the left boundary.

The linear flow L should take $G(A)$ to $G(B)$ so that $LG(A) = G(B)$ as required by Eq. (4). These properties are incorporated in our complete map G,

$$x_b = \phi(y_a) \,,$$
$$y_b = \{\mu + \gamma \bar{x}(x_a, y_a)\} y_a/y_0 + \epsilon f(y_a) \,, \quad (15)$$

where γ is a positive constant and where we now consider $\bar{x}$ as a function of x_a and y_a. In other words, given a point (x_a, y_a) we compute $\bar{x}$ by inverting Eq. (15),

$$\bar{x}(x_a, y_a) = x_a \left(\lambda_s/\lambda_u\right)^{-n(y_a)} y_0/y_a \,. \quad (16)$$

Geometrically, a curve on Σ_a with a fixed value of $\bar{x}$ gets mapped to Σ_b precisely the same way that the unstable manifold does for a value of μ shifted by an amount $\gamma\bar{x}$. See Fig. 4. Computation shows that G defined by (16) satisfies boundary conditions (4) and (6), where $\phi(y_a)$ and $\bar{x}(x_a, y_a)$ are given by (13) and (17) respectively and $f(y_a)$ satisfies (10), (11).

Now that a local and global mapping have been defined we can specify the dynamics of a point $(x, y \neq \lambda_u y_0) \in \Sigma_a$: the next return of the point (x, y) is given by $L^m G(x, y)$ where m is the smallest number of iterations of L needed to map the point $G(x, y) \in \Sigma_b$ to Σ_a. The dynamics of a point $(x, \lambda_u y_0) \in \Sigma_a$ on the upper boundary is given by the dynamics of the corresponding point $(\lambda_s^{-1} x, y_0) \in \Sigma_a$ on the lower boundary. (In this way the orbits through both of these points are considered to have the same number m of iterations of L.) In what follows we consider the map G with the expressions (13) and (17) for $\phi(y)$ and $\bar{x}(x, y)$, respectively. An explicit expression for $f(y)$ will not be needed.

3. Primary tangencies

A primary tangency occurs when the unstable manifold on Σ_a with $x_a = 0$ arrives at Σ_b tangent to the stable manifold $y_b = 0$ under the global map G. This occurs for points $(0, y^*) \in \Sigma_a$ at parameters (μ^*, ϵ) when

$$\mu^* y^*/y_0 + \epsilon f(y^*) = 0 \,,$$
$$\mu^*/y_0 + \epsilon f'(y^*) = 0 \,. \quad (17)$$

These equations are most easily understood graphically. One plots $\mu y/y_0$ and $-\epsilon f(y)$ as functions of y
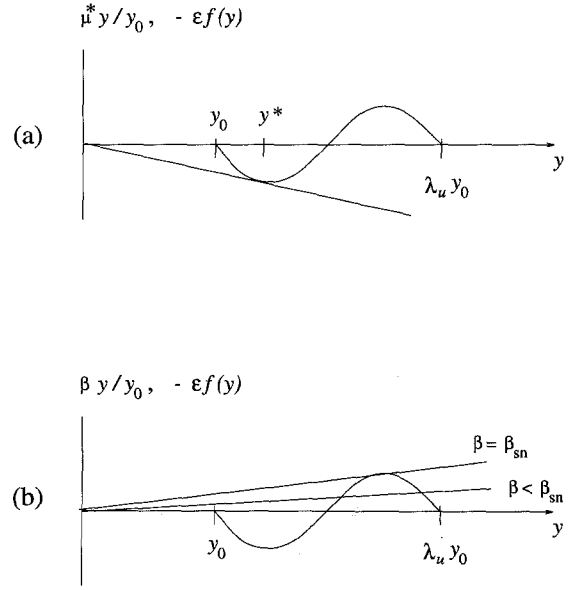

Fig. 5. (a) A graphical solution to (18) yields the values y^* and μ^* in which the stable and unstable manifolds of the limit cycle are tangent. For the solution shown $\mu^* < 0$. Another tangency occurs when $\mu > 0$. (b) A graphical solution to (23) yields the values of y and β for simple fixed points. At the tangency given by $\beta = \beta_{sn}$ a single orbit appears which splits into two orbits as β decreases.

on the same plot. With ϵ fixed at some non-zero value and $f(y)$ of the form depicted in Fig. 5a, the two curves $\mu y/y_0$ and $-\epsilon f(y)$ are tangent at two different values of μ^*, one positive and one negative. Note that the two values of y^* are the solutions to

$$y f'(y) = f(y) \,, \quad (18)$$

independent of μ. Given a solution y^* to Eq. (19) the value μ^* is given by

$$\mu^* = -\epsilon \frac{y_0}{y^*} f(y^*) \,. \quad (19)$$

In fact since the two roots y^* of (19) are independent of μ and ϵ the curves of homoclinic tangency (given by (20)) are readily identified as two straight lines in the (μ, ϵ) parameter plane. The lines have opposite signed slopes and form a wedge emanating from the origin ($\mu = 0$, $\epsilon = 0$).

4. Simple fixed points

The simplest periodic orbits of the flow are the trajectories which link up with themselves after only one pass through the global region of the flow. These correspond to fixed points $(x, y) \in \Sigma_a$ of our mapping which satisfy $(x, y) = L^m G(x, y)$, or more explicitly

$$x = \lambda_s^m \phi(y),$$
$$y = \lambda_u^m \left\{ \left[\mu + \gamma \bar{x}(x, y) \right] y/y_0 + \epsilon f(y) \right\}. \tag{20}$$

The substitution of the first equation $x = \lambda_s^m \phi(y)$ into the second equation yields an equation for y decoupled from x,

$$y = \lambda_u^m \left\{ \left(\mu + \gamma x_0 \lambda_s^m \right) y/y_0 + \epsilon f(y) \right\}. \tag{21}$$

Notice that because $\bar{x}(x, y) = x_0 \lambda_s^m$ is constant for fixed points of a given m on Σ_a, these fixed points lie on the same curve (15).

For graphical interpretation, Eq. (22) can be re-expressed as

$$\beta y = -\epsilon f(y), \tag{22}$$

where

$$\beta = \mu/y_0 - \left(y_0/\lambda_u^m - \gamma x_0 \lambda_s^m \right) /y_0. \tag{23}$$

We are primarily interested in the behavior of the fixed points as μ is varied through zero creating and destroying the primary tangencies. For this reason we continue to consider ϵ fixed and μ variable.

A plot of βy and $-\epsilon f(y)$ as functions of y on the same graph is shown in Fig. 5b. The intersections of the two curves correspond to fixed-point solutions to (23). As μ varies from positive to negative for large enough m the slope β of the curve βy also goes from positive to negative. A fixed point first appears as the curves become tangent at a positive β value. This fixed point splits in two after the tangency as β decreases. At $\beta = 0$, one of the fixed points passes through the top boundary $y = \lambda_u y_0$ of the return section, and another fixed point simultaneously appears at the lower boundary, $y = y_0$. Since the linear map L maps the lower boundary point to the upper, the two fixed points are identified with the same periodic cycle in the flow. As β decreases further the two distinct

fixed points merge again in a second saddle-node tangency and disappear. Thus as μ varies from positive to negative, two cycles are created in a saddle-node bifurcation and then the same two cycles merge and are destroyed in another saddle-node bifurcation.

Now we find where the saddle-node bifurcations occur relative to the primary homoclinic tangencies. The saddle nodes occur when

$$\beta = -\epsilon f'(y), \tag{24}$$

and a simple computation shows that the corresponding fixed point $(\lambda_s^m \phi(y), y)$ is also given by a solution of Eq. (19). (Thus the fixed point at the saddle-node bifurcation has $y = y^*$, the same y value yielding a primary tangency, although the x and μ values differ.) Combining Eqs. (19), (20) and (25) evaluated at $y = y^*$, we find that at a saddle-node bifurcation $\beta_{\text{sn}} = \mu^*/y_0$, and therefore from (24) the value μ_{sn} of μ at the bifurcation is

$$\mu_{\text{sn}} = \mu^* + \frac{1}{\lambda_u^m} \left\{ y_0 - \gamma x_0 (\lambda_u \lambda_s)^m \right\}. \tag{25}$$

Thus the saddle-node bifurcations converge to μ^* (see Eq. (20)) from above with increasing m for the case $\lambda_u \lambda_s < 1$, while they converge from below for $\lambda_u \lambda_s > 1$ ($\gamma > 0$).

Fig. 6 depicts the curves of saddle-node bifurcations in the (μ, ϵ) parameter space given by Eq. (26) for $\lambda_u \lambda_s < 1$. The curves accumulate upon the wedge formed by the primary homoclinic tangency curves (Eq. (20)). Also shown is a period T versus μ sketch for the limit cycles along a fixed ϵ parameter path. Since two orbits born near one tangency are the same two that annihilate at the other the orbits trace out an *isolated* loop or 'bubble' in this plot. Each isolated bubble corresponds to limit cycles which pass through the local regime under L the same integral number (m) of times. If the primary limit cycle has a period τ then the separation between bubbles along the T-axis is approximately τ (see for example Gaspard and Wang [4]).

Consideration of the phase space geometry of the flow can provide further insight into the appearance of the isolated bubbles in Fig. 6. Note that a simple limit cycle is constrained to remain within the approx-

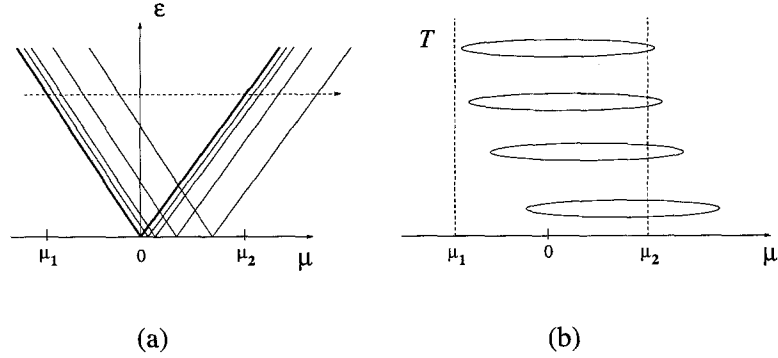(a)   (b)

Fig. 6. Shown in (a) are curves of saddle-node bifurcations in the (μ, ϵ) parameter space which converge upon the leading tangency curve (bold curve, $\mu > 0$) and the trailing tangency curve (bold curve, $\mu < 0$). Shown in (b) is a sketch of period T versus μ for the limit cycles along a parameter path with fixed ϵ (dashed line shown in (a)). The leading tangency occurs at μ_2, while trailing occurs at μ_1. For both (a) and (b) $\lambda_u \lambda_s < 1$.

imately toroidal-shaped phase space region bounded by the stable and unstable manifolds of the primary limit cycle. To smoothly deform a simple cycle in such a way as to increase or decrease the number of turns it makes about the primary cycle would force the simple cycle to cross at least one of the invariant manifolds of the primary limit cycle—something that cannot occur. Therefore orbits represented by a particular bubble cannot be smoothly deformed by the variation of parameters (μ and ϵ) into orbits represented by other bubbles, ensuring the isolation of the bubbles in Fig. 6. However, should the parameters of a system stray far enough from the $\mu = 0$, $\epsilon = 0$ case it is possible, if not likely, that the global manifolds of the primary cycle will evolve far enough from the assumed configurations depicted in Fig. 1 that the geometry no longer provides a sufficient constraint and orbits from one bubble might deform smoothly into orbits from other bubbles.

5. Stability of simple fixed points

An eigenvalue, Λ, of a simple fixed point $(x, y) \in \Sigma_a$ given by (21) satisfies

$$\Lambda^2 - T\Lambda + D = 0 \,, \tag{26}$$

where

$$D = -\gamma(\lambda_u \lambda_s)^m (x_0 \log \lambda_s) / (y_0 \log \lambda_u) \,,$$

$$T = F'_\mu(y) + D \,, \tag{27}$$

and

$$F'_\mu(y) = \lambda_u^m \left\{ \left(\mu + \gamma\lambda_s^m x_0 \right) / y_0 + \epsilon f'(y) \right\} \,. \tag{28}$$

From the elimination of β between Eqs. (24) and (25) we see that the saddle-node bifurcation occurs when $F'_\mu(y) = 1$. This implies that the eigenvalues for the fixed point at the saddle node are $\Lambda_{sn} = 1, D$. Note that D is positive since $\log \lambda_s < 0$ and $\gamma > 0$. Thus when $\lambda_u \lambda_s < 1$ and for large enough m the eigenvalue D is less than unity and one of the two emerging orbits (the node) will be stable, while when $\lambda_u \lambda_s > 1$ the orbits are unstable.

The stable orbit can lose stability through a period-doubling instability. This occurs when one eigenvalue is -1. The other eigenvalue is $-D$ which is also negative and has a small magnitude, $|D| \sim (\lambda_u \lambda_s)^m$. This instability can be described graphically by considering the expression $F'_\mu(y)$ when $\Lambda = -1$. When $\Lambda = -1$ Eq. (27) yields $1 + T + D = 0$ which when combined with expressions (28) produces

$$F'_\mu(y) = -1 + 2\gamma(\lambda_u \lambda_s)^m \frac{x_0 \log \lambda_s}{y_0 \log \lambda_u} \,. \tag{29}$$

The substitution of the definition of β (Eq. (24)) and the definition of $F'_\mu(y)$ (Eq. (29)) into Eq. (30) yields

$$\beta = -\epsilon f'(y) - Q/\lambda_u^m \,, \tag{30}$$

where

$$Q = 2 - 2\gamma(\lambda_s\lambda_u)^m (x_0 \log \lambda_s)/(y_0 \log \lambda_u) \,. \quad (31)$$

Note that Q is positive and recall that fixed points satisfy Eq. (23), $\beta y = -\epsilon f(y)$. For large m Eq. (31) approaches Eq. (25) and graphically the period-doubling fixed point moves closer towards the point of saddle-node tangency. To determine which of the two orbits appearing after the saddle-node bifurcation undergoes period doubling we refer to Fig. 5b. The intersection point at which the slope β of the straight line is *less* than the slope of the curve $-\epsilon f'(y)$ corresponds to the fixed point that period doubles (as given by Eq. 31). Thus the left intersection point on the $\beta < \beta_{sn}$ curve of Fig. 5b undergoes period doubling.

In summary, at the first saddle node ($\mu > 0$) the stable orbit has a smaller y value than the saddle and then shortly loses stability through period doubling. The now unstable orbit eventually becomes stable again in a reverse period-doubling bifurcation just prior to disappearing in the final saddle-node bifurcation ($\mu < 0$). During the approach to the final saddle-node bifurcation the node orbit now has the larger y value (independent of the sign of ϵ).

6. The $\epsilon = 0$ case

An important special case to consider is when the stable and unstable manifolds have a "flat" tangency, as when $\epsilon = 0$. In the flow to be considered in Section 7 the manifolds behave this way as a consequence of rotational symmetry. In this flow symmetry allows for the variable associated with the phase of the limit cycle to decouple from the equations for the remaining two variables. This effectively reduces the three-dimensional flow to a flow on a plane. (This reduction to a planar flow arises frequently in the analysis of many normal forms [9].) The upper sketch of Fig. 1 illustrates the relation of such a planar flow to the three-dimensional flow at the homoclinic connection. In the planar flow the connection is a homoclinic loop to a saddle fixed point. It is well known that appropriate perturbations to a planar flow with a homoclinic loop give rise to a limit cycle (see [14]). Fur-

ther a limit cycle in the planar flow corresponds to an invariant two-torus in the three-dimensional flow.

For the unperturbed flow considered in Section 7, the two frequencies of the torus remain independent and frequency-locking cannot occur. Perturbations which break the rotational symmetry induce frequency-locking. We now demonstrate that the behavior of our map for $\mu > 0$ and $\epsilon = 0$ is consistent with the presence of an invariant torus in the corresponding flow.

For $\epsilon = 0$ and μ positive and small enough, the invariant torus should intersect Σ_a and Σ_b. The intersection should appear as an invariant curve on each of these return sections (recall that Σ_a and Σ_b are small sections unlike the section shown in Fig. 1). Repeating the analysis in Sections 4 and 5 with $\epsilon = 0$ we find that the simple fixed points of our map for a given m correspond to the entire set of points (x, y) on the curve (15) with $\bar{x} = x_0 \lambda_s^m$ at the isolated value of μ,

$$\mu = \frac{1}{\lambda_u^m} \left\{ y_0 - \gamma x_0 (\lambda_u \lambda_s)^m \right\} \,, \quad (32)$$

and that these points are stable when $\lambda_u \lambda_s < 1$ and unstable when $\lambda_u \lambda_s > 1$. This invariant curve of fixed points is the intersection of the torus with Σ_a. The ratio of frequencies on the torus is $1 : (m + k)$, where k rotations about the primary periodic orbit occur during the global portion of the flow which takes a point from Σ_a to Σ_b. For other values of μ the torus still exists, but the ratio of its frequencies (its rotation number) is of a different form.

When ϵ is non-zero, only two periodic orbits persist from the continuum of periodic orbits as demonstrated in Section 4. This is consistent with frequency-locking on the torus in the three-dimensional flow. These two orbits persist in a resonance tongue in the (μ, ϵ) parameter space. The resonance tongue with rotation number $1/(m + k)$ branches off the μ-axis at a value given by (33). With increasing m the tongues approach the (μ, ϵ) curves corresponding to leading and trailing homoclinic tangencies. The tongues for saddle-node bifurcations of the simplest fixed points are sketched in the (μ, ϵ) plane in Fig. 6a.

7. A numerical example

Laing [12] studies the following equations:

$$\dot{q} = q(\eta + i\omega + \alpha z + \kappa_1 \,|q|^2 + \kappa_2 z\bar{q}) + \kappa_3 z^3 \,,$$
$$\dot{z} = \nu - z^2 - |q|^2 \,, \qquad (33)$$

where $q \in \mathbb{C}$; $\omega, \alpha, \kappa_1, \kappa_2, \kappa_3, z \in \mathbb{R}$; $i^2 = -1$, and ν and η are real parameters. When $\kappa_2 = \kappa_3 = 0$ the equations are a rescaled truncation of the normal form of the saddle-node/Hopf bifurcation [3,9] with α and κ_1 chosen real. In this case, the flow of Eq. (34) is axisymmetric about the z-axis, and the z-axis is also dynamically invariant. As a consequence of the axisymmetry of the flow, the substitution $q = re^{i\theta}$ yields the decoupled equations

$$\dot{r} = r(\eta + \alpha z + \kappa_1 r^2) \,,$$
$$\dot{z} = \nu - r^2 - z^2 \,,$$
$$\dot{\theta} = \omega \,. \qquad (34)$$

Since the $\dot{r}$ and $\dot{z}$ equations do not depend on θ, the system can be analyzed as a planar vector field. A non-zero κ_2 breaks the axisymmetry of the flow, while a non-zero κ_3 breaks the z-axis invariance. In these cases the equations no longer decouple and the full three-dimensional flow (34) must be considered.

At the parameter values

$$(\eta, \nu) = (-\alpha(1 + \alpha)/2\kappa_1, \alpha(2 + \alpha)/4\kappa_1^2), \qquad (35)$$

the Jacobian matrix of the planar vector field evaluated at the fixed point $(r, z) = (\sqrt{\alpha/2\kappa_1^2}, \alpha/2\kappa_1)$ has a repeated, non-semisimple eigenvalue of 0 and thus undergoes a Takens–Bogdanov bifurcation. The relevant corresponding bifurcation set and phase portraits for Eq. (35) are shown in Fig. 7. In the planar phase portraits r is plotted horizontally and z vertically. To obtain the full three-dimensional flow, each sketch must be rotated about the z-axis. (Figs. 7–11 were obtained using the software AUTO [2].)

Note that in the region of parameter space enclosed by the curves of secondary Hopf and homoclinic bifurcations, there exists a periodic orbit in the planar flow which corresponds to a two-torus in the three-dimensional flow. Because the flow is axisymmetric,

the two frequencies associated with motion on the torus are independent, and there is no frequency locking. The homoclinic bifurcation occurs as the torus collides with a limit cycle (a fixed point in the planar representation) whose multipliers satisfy $0 < \lambda_s \lambda_u < 1$. This is the $\epsilon = 0$ case considered in Section 6. We emphasize that our model map addresses the dynamics associated with systems which lie near a point on the curve of homoclinic bifurcation of Fig. 7 and therefore does not capture behavior near the other bifurcation curves (nor in particular near the TB point).

7.1. Breaking the axisymmetry

We now examine the case when $\kappa_2 \neq 0$, but κ_3 is still zero. This corresponds to setting ϵ non-zero in our model map and causes the curve of homoclinic bifurcations in Fig. 7 to split into a region bounded by the leading and trailing homoclinic tangencies, as shown in Fig. 8. It also causes locking on the torus, which is evident by the appearance of a countable infinity of resonance (Arnol'd) tongues.

A few of these tongues (with rotation numbers of the form $1/n$) are shown in Fig. 9, together with the curves already shown in Fig. 8. The edges of the resonance tongues are saddle-node bifurcations of periodic orbits, and within each tongue there are two orbits with the specified rotation number.

Figs. 7–9 serve to illustrate how the homoclinic bifurcation to a limit cycle that we have analyzed in Sections 2–6 can appear in an analysis of equations with approximate S^1 symmetry (as often arises in normal forms involving a Hopf interaction). However, Fig. 9 should be compared to Fig. 6a with caution as the parameters being varied in the respective plots do not directly correspond. The relations between parameters of the flow (ν, κ_2, η) and those in the map (μ, ϵ) are as follows. The variation of the parameter μ in the map causes the unstable and stable manifolds to pass through one another. This is accomplished in the flow by varying ν while fixing κ_2 and η. Thus the (loose) identification of μ with ν is appropriate. The parameters ϵ (in the model map) and κ_2 (in the flow) can similarly be identified; increasing these from zero causes the stable and unstable manifolds to buckle. A
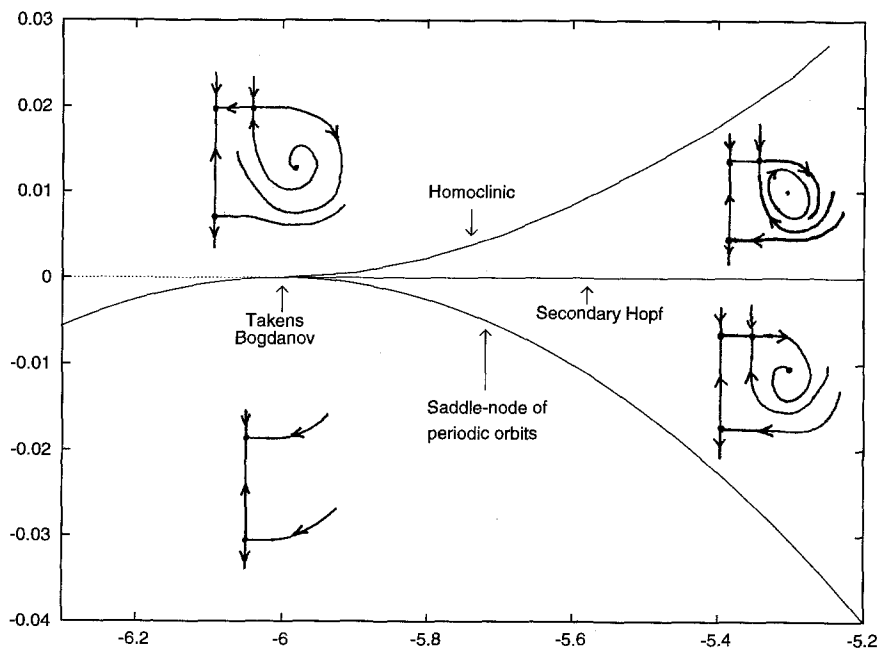
Fig. 7. Bifurcation set and phase portraits for Eqs. (35). The horizontal axis is η, while the vertical is $\nu - \eta^2/16 + \eta/4$. The phase portraits have r plotted horizontally and z vertically. To obtain the full three-dimensional flow, each sketch must be rotated about the z-axis (the vertical line at the left of each sketch). Parameter values are $\alpha = 3, \kappa_1 = 1$.
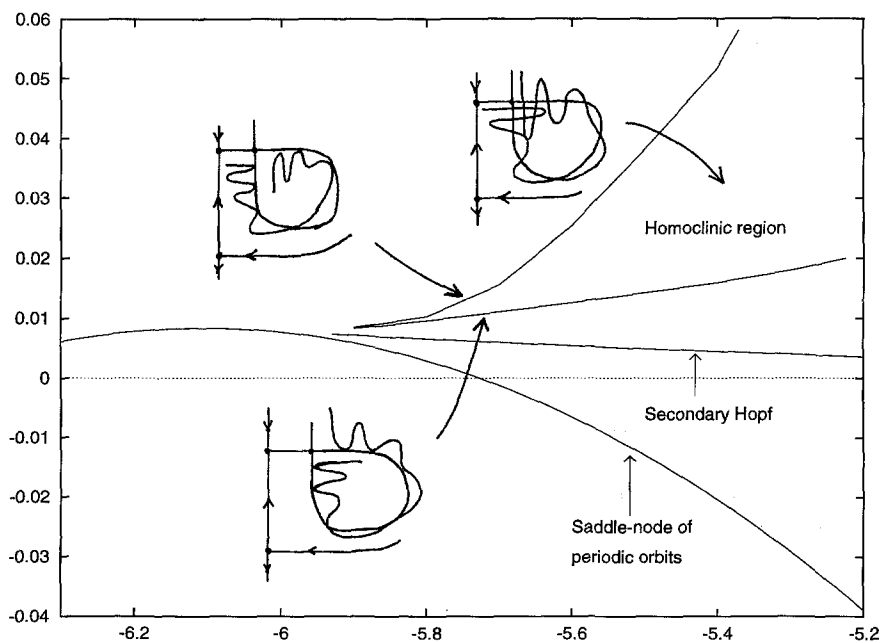

Fig. 8. Homoclinic region and phase portraits near the homoclinic region for Eqs. (34), with parameter values $\alpha = 3$, $\omega = 3.75$, $\kappa_1 = 1$, $\kappa_2 = 0.2$, $\kappa_3 = 0$. The phase portraits show the dynamics induced on a cross section of the flow chosen to include the z-axis. The horizontal axis is η, while the vertical is $\nu - \eta^2/16 + \eta/4$.
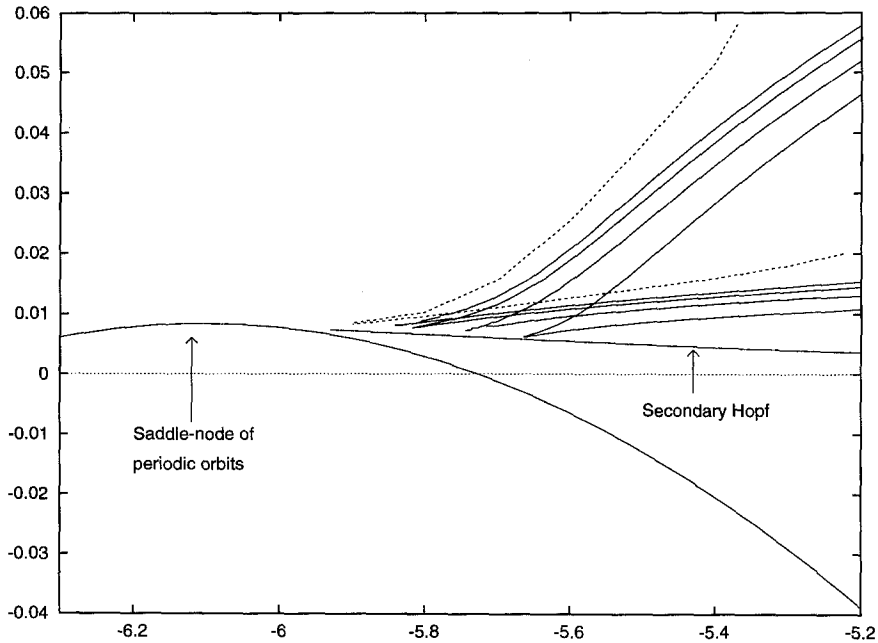
Fig. 9. Boundaries of the resonance tongues with rotation numbers 1/5, 1/6, 1/7 and 1/8, together with the edges of the homoclinic region. The tongues are seen to accumulate on the edges of the homoclinic region (shown dashed) as the rotation number tends to zero. Parameter values and axes are the same as in Fig. 8.

third parameter in the flow η does not have a direct analogue in the map. The variation of this parameter moves the system away from the Takens–Bogdanov point and controls the size of the primary limit cycle. Since our map is based on a limit cycle with fixed size, the plot of μ versus ϵ in Fig. 6a would correspond to a planar cross section at constant η (not shown) through the parameter space (ν, κ_2, η) of the flow. Fig. 9 is a section at fixed κ_2.

To verify that the simplest periodic orbits form closed loops or bubbles in the period versus parameter diagrams as predicted in Section 4, we plot in Fig. 10 the period versus ν at $\eta = -5.5$, $\kappa_2 = 0.2$ of several limit cycles for Eq. (34). What appear to be horizontal line segments in Fig. 10 are in fact closed bubbles. One such bubble is shown in Fig. 11. Fig. 10 should be compared with Fig. 6b.

7.2. Breaking the axis-invariance

When κ_3 is zero, the z-axis is dynamically invariant. The number of times a periodic orbit links the z-axis

is therefore invariant. Thus the closed loops in Fig. 10 may not be surprising. However, the trajectories of the periodic orbits of Fig. 10 lie in a doughnut region of phase space that is well separated from the z-axis as noted in Section 4. Thus whether or not the z-axis is invariant is not directly relevant for the behavior of the periodic orbits formed in the homoclinic bifurcation of the primary cycle. This can be demonstrated by setting $\kappa_3 \neq 0$ and producing a plot similar to Fig. 10. This is done in Ref. [12] and the results are qualitatively identical to the axis-invariant case, i.e. the periodic orbits form closed loops in period-parameter space.

8. Concluding remarks

We have considered a homoclinic tangency to a limit cycle in which the stable and unstable manifolds pass through two successive tangencies. The two tangencies occur close together in parameter space and we have been able to connect up orbits appearing at one tangency with those at another. For both the numerics
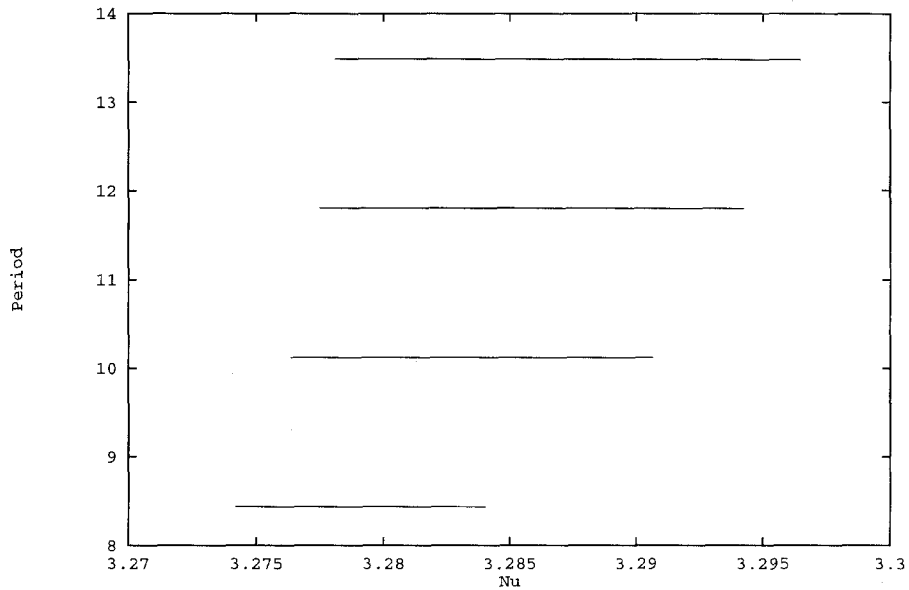
Fig. 10. Plot of period versus ν at $\eta = -5.5$ for periodic orbits corresponding to tongues with rotation numbers 1/5, 1/6, 1/7 and 1/8, for Eqs. (34) with parameters as in Fig. 8. (The 1/5 tongue has the lowest period, the 1/8, the highest.) What appear to be straight lines are actually closed loops.
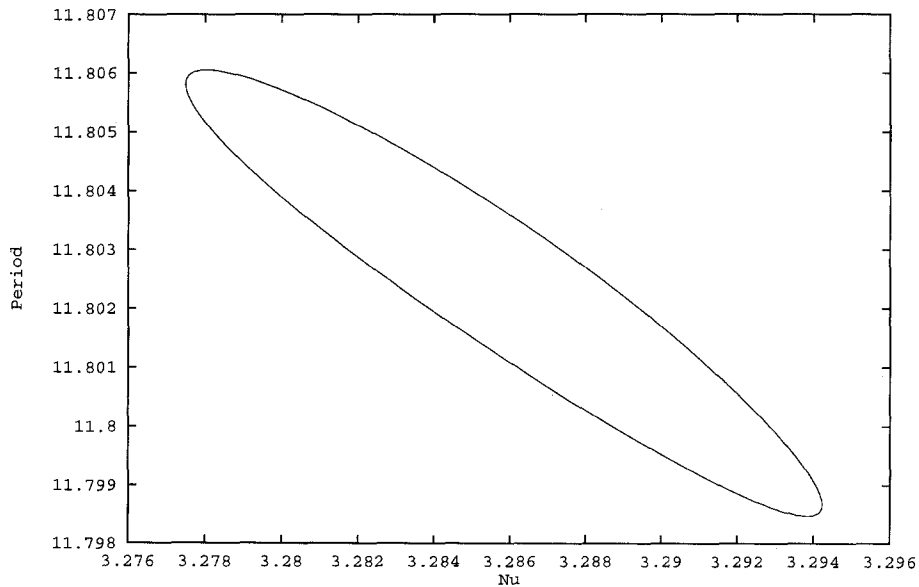

Fig. 11. Enlargement of the plot (period versus ν at $\eta = -5.5$) for the tongue with rotation number 1/7 shown in Fig. 10. Corresponding plots for other tongues are qualitatively the same demonstrating that the horizontal line segments of Fig. 10 are actually closed loops. Parameters as in Fig. 8.

of a flow and our model map, a plot of orbit period versus a parameter path through the two tangencies yields closed bubbles.

The Šil'nikov–Hopf bifurcation [10] provides another example where two tangency curves come together in parameter space and the associated saddle-node bifurcations at the separate tangencies may be linked together. Period versus parameter plots in this situation also show the accumulation of saddle-node bifurcations on homoclinic tangencies, but in this case the orbits are linked by a single curve which zigzags in a bifurcation diagram similar to the Šil'nikov case [7]. This difference can be attributed to the global arrangements of the manifolds of the periodic orbit.

The global bifurcation we have studied can be interpreted as a collision between a two-torus and the limit cycle. In a similar situation, Kirk [11] studies a torus which collides with two fixed points. When the fixed points lie on an invariant axis the orbits are forced to have fixed rotation numbers and the resulting period versus parameter plots have closed bubbles much as in our Fig. 6. Unlike our case, terms that break the invariance of the axis cause the bubble diagrams to break open. Our diagrams retain the closed bubbles as a consequence of the global arrangements of the stable and unstable manifolds.

Finally, we addressed the global bifurcation from a qualitative and geometric perspective with the hope that we have captured the behavior of a large class of systems. Analytic results providing parameter values for the accumulation of 'wedges' bounded by saddle-node bifurcations on a homoclinic region have been obtained in several specific systems (Greenspan and Holmes [8], Chow, Hale and Mallet-Paret [1]). These results have been derived using Melnikov theory for which an analytic expression for the unperturbed homoclinic orbit is needed.

Acknowledgments

References

[1] S.N. Chow, J.K. Hale and J. Mallet-Paret, An example of bifurcation to homoclinic orbits, J. Diff. Eqns. 37 (1983) 351–373.

[2] E.J. Doedel and J.P. Kernevez, AUTO: Software for continuation and bifurcation problems in ordinary differential equations. Report, Applied Mathematics, California Institute of Technology (1986).

[3] P. Gaspard, Local birth of homoclinic chaos, Physica D 62 (1993) 94–122.

[4] P. Gaspard and X.-J. Wang, Homoclinic orbits and mixed-mode oscillations in far-from-equilibrium systems, J. Stat. Phys. 48 (1987) 151–199.

[5] N.K. Gavrilov and L.P. Šil'nikov, On three-dimensional dynamical systems close to systems with a structurally unstable homoclinic curve. I., Math. USSR-Sb. 17 (1972) 467–485.

[6] N.K. Gavrilov and L.P. Šil'nikov, On three-dimensional dynamical systems close to systems with a structurally unstable homoclinic curve. II., Math. USSR-Sb. 19 (1973) 139–156.

[7] P. Glendinning and C. Sparrow, Local and global behavior near homoclinic orbits, J. Stat. Phys. 35 (1984) 645–696.

[8] B.D. Greenspan and P.J. Holmes, Repeated resonance and homoclinic bifurcations in a periodically forced family of oscillators, SIAM J. Math. Anal. 15 (1983) 69–97.

[9] J. Guckenheimer and P.J. Holmes, Nonlinear Oscillations, Dynamical Systems and Bifurcations of Vector Fields (Springer, Berlin, 1990).

[10] P. Hirschberg and E. Knobloch, Šil'nikov–Hopf bifurcation, Physica D 62 (1993) 202–216.

[11] V. Kirk, Merging of resonance tongues, Physica D 66 (1993) 267–281.

[12] C. Laing, Merging of resonance tongues near the saddle-node/Hopf bifurcation, M.Sc. thesis, University of Auckland (1994).

[13] S. Newhouse, The abundance of wild hyperbolic sets and non-smooth stable sets for diffeomorphisms, Publ. Math. IHES 50 (1979) 101–151.

[14] S. Wiggins, Global Bifurcations and Chaos (Springer, Berlin, 1988).